Unlocking High Capacity and Fast Na⁺ Diffusion of H$_x$CrS$_2$ by Proton-Exchange Pretreatment

Joseph W. Stiles, Anna L. Soltys, Xiaoyu Song, Saul H. Lapidus, Craig B. Arnold, and Leslie M. Schoop*

This study presents a new material, "H$_x$CrS$_2$" (denotes approximate composition) formed by proton-exchange of NaCrS$_2$ which has a measured capacity of 728 mAh g^{-1} with significant improvements to capacity retention, sustaining over 700 mAh g^{-1} during cycling experiments. This is the highest reported capacity for a transition metal sulfide electrode and outperforms the most promising proposed sodium anodes to date. H$_x$CrS$_2$ exhibits a biphasic structure featuring alternating crystalline and amorphous lamella on the scale of a few nanometers. This unique structural motif enables reversible access to Cr redox in the material resulting in higher capacities than seen in the parent structure which features only S redox. Pretreatment by proton-exchange offers a route to materials such as H$_x$CrS$_2$ which provide fast diffusion and high capacities for sodium-ion batteries.

1. Introduction

Unsustainable mining and limited availability of lithium-ion battery materials have created a driving need to develop alternatives such as sodium hosts.[1–4] The development of suitable anode materials remains a major challenge facing sodium-ion battery development. Graphite, the prototypical lithium-ion battery anode, does not reversibly intercalate sodium.[2] Among the known sodium anodes, antimony with a fluoroethylene carbonate (FEC) additive has been noted as the most promising, maintaining a capacity of 576 mAh g^{-1} over 160 cycles at charge

rates of C/2.[5] Sn$_4$P$_3$ with FEC additive has been shown to have higher capacities than antimony (718 mAh g^{-1}), although at lower rates of about C/10.[6] A number of transition metal oxides and sulfides have also been investigated in part due to their high cycling stability. Interest in sulfide electrodes has increased due to better reversibility of the conversion to Na$_2$S compared with Na$_2$O.[7–9] These promise high capacities but have suffered from low coulombic efficiency due to volume expansion during cycling.[5] Here we avoid such expansion through pretreatment to form new phases which limit volume change.

Transition metal dichalcogenides (TMDs) such as TiS$_2$, were among the first materials studied as intercalation cathodes during the initial development of Li-ion batteries.[10] The conversion reactions between the guest ion and the chalcogenide to form A$_2$X (A = Li, Na; X = S, Se, Te) lead to the capacity limiting volume expansion.[11–14] However, the larger interstitial volume and weaker electrostatic interactions of the guest with the chalcogenide host remain benefits of using TMD electrodes, especially in the development of beyond-Li-ion batteries.[15] Efforts into studying the charge storage of sodium in transition metal sulfides have gained traction due to improved kinetics compared with oxides.[7] Van der Waals CrS$_2$ has been predicted to be a good intercalation host for both Na and Mg which may circumvent side reactions that plague TMD batteries but has not been isolated as a bulk phase.[7,16]

Shadike et al. identified delafossite NaCrS$_2$, which contains [CrS$_2$]$^-$ layers, intercalated by Na$^+$, as a potential sodium battery electrode material. They showed that it features electrochemically active sulfur rather than chromium.[17] They additionally observe "abnormal breathing" of the unit cell in which a contraction in the a axis is seen rather than the c axis due to migration of Cr into the Na vacancies. However, the study was limited to the (de)intercalation of 0.5 formula units of Na into and out of the electrode which limited the observed capacity.[17] The anionic redox chemistry of NaCrS$_2$ makes it a prime candidate for further study. Several recent Li-ion electrode candidates exhibit coupled cationic/anionic reversible redox during ion (de)intercalation.[9,18–22] This cationic/anionic coupling reduces structural distortions during cycling by affecting electrons in the anion non-bonding orbitals rather than pulling from a bonding orbital and destabilizing the electrode structure.[23] Additionally, accessing both cationic and anionic redox allows

J. W. Stiles, A. L. Soltys, X. Song, L. M. Schoop
Department of Chemistry
Princeton University
Princeton, NJ 08540, USA
E-mail: lschoop@princeton.edu
J. W. Stiles, C. B. Arnold, L. M. Schoop
Princeton Institute for the Science and Technology of Materials
Princeton University
Princeton, NJ 08540, USA
S. H. Lapidus
X-ray Science Division
Advanced Photon Source
Argonne National Laboratory
9700 S. Cass Ave, Argonne, IL 60439, USA
C. B. Arnold
Department of Mechanical and Aerospace Engineering
Princeton University
Princeton, NJ 08540, USA

**ADVANCED
SCIENCE NEWS**

www.advancedsciencenews.com

**ADVANCED
MATERIALS**

www.advmat.de

for higher capacities than would otherwise be achievable. We here seek to alter the structure of $NaCrS_2$ so higher reversible capacities can be achieved, possibly through coupling of cationic and anionic redox.

Our group recently demonstrated that proton-exchange of $NaCrS_2$ to form "H_xCrS_2" ($0 < x < 1$) results in structural rearrangements including the migration of Cr into the Na vacancies.[24] This proton-exchanged phase features alternating crystalline and amorphous layers as a result of the Cr migration. The actual composition of these layers is closer to $H_xCrS_{1.9}$ and $H_yCrS_{2.4}$ respectively and is discussed in depth below. Raman studies performed by Song et al. show the presence of a S–H stretch that corresponds to the strong S–H bond in calculated spectra for $H_{0.5}CrS_2$. This additionally, shows that the protons are strongly bound to the structure and unlikely to contribute to the material's capacity. Previous studies on $ACrS_2$ (A = Li, Na) have shown that the occurrence of Cr-migration during cycling is one of the main contributors to capacity fade.[11,17] By enabling Cr-migration to occur during the material processing, we can study its electrochemical performance in the absence of structural rearrangements. The biphasic nature of this new material also allows for the study of complex ion dynamics during the intercalation process.

Although mechanical processing to optimize size and morphology of electrode particles has been a recent focus of electrode research, less attention has been directed toward chemical methods to affect stacking order or initial composition.[25] Cheng et al. have recently demonstrated that exfoliation and re-stacking of $LiCoO_2$ and $LiNi_{1/3}Mn_{1/3}Co_{1/3}O_2$ (NMC) result in marked changes to their electrochemical behavior including increased capacity and in the case of NMC, the evolution of additional redox events.[26,27] Similarly, it has been demonstrated that exfoliated and re-stacked MoS_2 pellets have improved Mg^{2+} diffusion which is further improved if the sheets are reassembled around an interlayer spacer such as polyethylene oxide.[28] SnS_2 and VS_2 have also recently been demonstrated as promising anode materials when composited with graphene, FeS_2, Bi_2S_3, or other materials which greatly improves their performance.[29–33] The engineering of these interlayers allows materials such as SnS_2 which has previously exhibited relatively poor performance to access remarkably high capacities and rates. These studies look to layer stacking and interlayer engineering as a tunable point for electrode development. Recent work from Butala et al. discusses the charge storage mechanism of $Li-FeS_2$ cells in which a significant structural change occurs after the first discharge to produce a new phase which then behaves more as an intercalation electrode.[34] This highlights the importance of learning from intermediate phases to inform research into novel electrodes. The following work builds off of these ideas to identify changes in the electrochemical behavior of chemically desodiated $NaCrS_2$.

Here we report that H_xCrS_2 has improved electrochemical behavior over a range of performance metrics. H_xCrS_2 exhibits faster evolution of redox features and higher current densities than $NaCrS_2$ which may allow for coupled cationic-anionic redox. Additionally, the material demonstrates fast sodium diffusion that is retained with cycling. This enables a high capacity of 728 mAh g^{-1} that is retained over long term cycling experiments, a twofold to threefold improvement over $NaCrS_2$. This

is the highest reported capacity for a bare transition metal chalcogenide electrode.[2,5] These capacities outperform those of antimony and the overall performance of H_xCrS_2 is comparable to Sn_4P_3.[5,6] H_xCrS_2 achieves such performance without the addition of dangerous and toxic fluorinated carbonates such as FEC. This is additionally achieved without any compositing with materials such as graphene or other chalcogenides which have been shown to improve capacity in SnS_2.[29–33] Future studies may show that composites of H_xCrS_2 can achieve even better performance. The results here presented suggest that soft chemical processing is a route to produce high rate and capacity electrodes.

2. Results

2.1. Biphasic Structure of H_xCrS_2

H_xCrS_2 features an altered stacking pattern with alternating crystalline and amorphous layers. Powder X-ray diffraction (XRD) measurements of $NaCrS_2$ and H_xCrS_2 in Figure S1, Supporting Information show an overall reduction in crystallinity after pretreatment. However, several key peaks remain visible in the pattern. Specifically, the (00l) and (110) peaks each shift to slightly higher angles due to the migration of Cr into the interlayer. The migration results in a change from the $NaCrS_2$ structure shown in **Figure 1**a to a new structure in Figure 1b which features Cr-S octahedra forming crystalline slabs, interspaced by an amorphous layer. These results are in agreement with transmission electron microscopy (TEM) studies performed by Song et al. which show alternating crystalline and amorphous layers.[24] Notably, the new material's structure is biphasic and ordered in that the repetition of the amorphous layer is periodic within the structure.

The alternating amorphous/crystalline structure of H_xCrS_2 is key to the results we report here. In the initial reports of the material, Song et al. demonstrate that the crystalline phase is Cr rich and the amorphous phase is Cr poor where the two exist in approximately a 1:1 ratio (based on high resolution scanning transmission electron microscopy measurements on single crystals) with each other. This indicates that roughly half of the Cr must have migrated out of the crystal lattice into the interlayer to form the amorphous phase. The crystalline stoichiometry is reported as $H_xCrS_{1.9}$ while the amorphous composition is $H_yCrS_{2.4}$ ($x > 0$, $y \geq 0$) and is closely related to the reported phase CrS_3.[24,35] Therefore "H_xCrS_2" refers only to an approximate stoichiometry of the actual material which can also vary based on the ratio between the crystalline and amorphous phases. Given this unusual combination of stoichiometries, the theoretical maximum capacity of the material would be ≈755.1 mAh g^{-1} corresponding to 3.3 Na per mol of active material assuming a 1:1 ratio of amorphous to crystalline phase. This calculation is based on the assumption of Cr^{3+} reduction to Cr^+ and total reduction of the persulfide dimer $(S_2)^{2-}$ to lattice sulfides $(S^{2-})_2$. Notably, a larger phase fraction of the amorphous phase can be expected to result in a higher theoretical capacity material due to the larger stoichiometric quantity of sulfur. By contrast, $NaCrS_2$ is theoretically capable of at most 3 Na per mol of active material and has a markedly
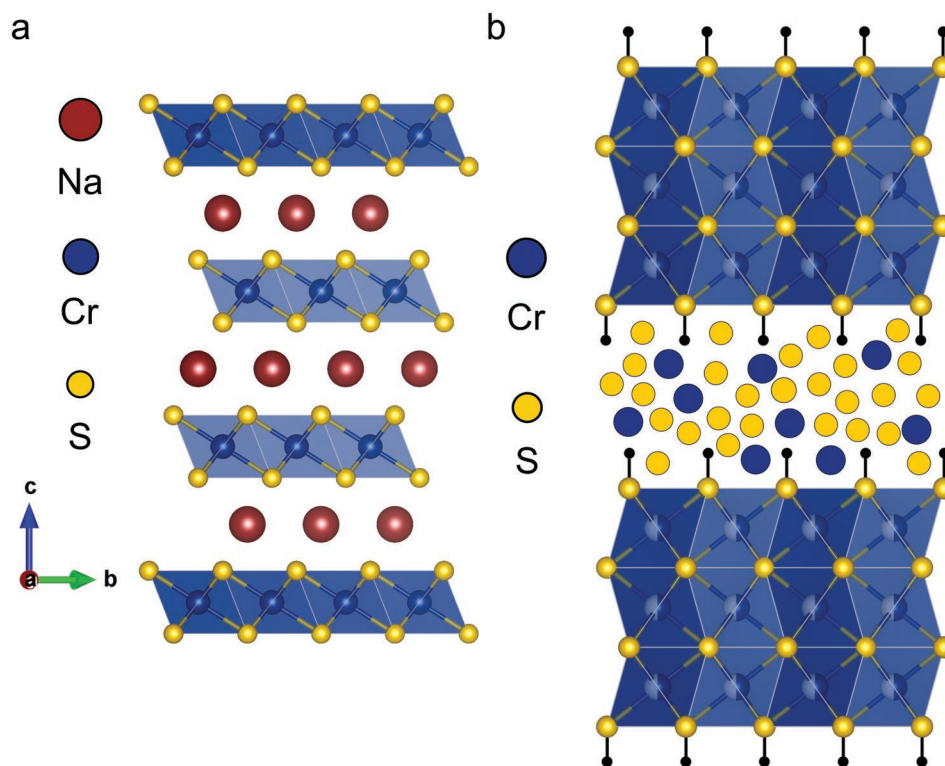
**ADVANCED
SCIENCE NEWS**

www.advancedsciencenews.com

**ADVANCED
MATERIALS**

www.advmat.de

Figure 1. Representative structures of $NaCrS_2$ and H_xCrS_2. a) Crystal structure of $NaCrS_2$ featuring CrS_2 layers interspaced with Na^+ undergoes significant structural rearrangement during proton-exchange to form b) H_xCrS_2. Cr migrates from the CrS_2 layers into Na^+ vacancies forming slabs reminiscent of CrS with an amorphous layer between the slabs. Powder XRD patterns for each phase are shown in Figure S1, Supporting Information.

lower measured capacity.[17] This demonstrates that the chemical processing and structural changes drive an increase in the theoretical capacity of the material.

2.2. Diffusion of Na^+ through H_xCrS_2 and Electrochemical Characterization

Amorphous materials are also known to feature faster ionic mobility than highly crystalline compounds.[36] To compare the diffusion of guest ions through $NaCrS_2$ and H_xCrS_2 we employed electrochemical impedance spectroscopy (EIS) to study the charged and discharged states of both materials. Equivalent circuit fits of the resultant Nyquist plots were used to determine the diffusion constants for the materials. Equivalent circuits adapted from Westerhoff et al. were used to fit the data.[37] Fits of the Warburg tail yielded a diffusion coefficient from which, diffusion constants could be calculated. A more thorough explanation of these calculations is provided in the Supplemental Information. The impedance plots and fits can be seen in **Figure 2** and it can be seen from the magnitude of the impedances that the discharged H_xCrS_2 features faster ionic diffusion. The diffusion constant for $NaCrS_2$ before any cycling was on the order of 10^{-12} cm^2 s^{-1} and after the first charge was on the order of 10^{-14} cm^2 s^{-1}. The diffusion constant for H_xCrS_2 before any discharge is similarly large, on the order of 10^{-14} cm^2 s^{-1}, but after the first discharge increases to 10^{-9} cm^2 s^{-1}. This high diffusion constant is reproducible

and retained over many cycles (Figures S5 and S6, Supporting Information).

It is additionally of note that the diffusion character exhibited by H_xCrS_2 differs from that of $NaCrS_2$. While $NaCrS_2$ Nyquist plots fit to a standard infinite Warburg, the H_xCrS_2 was fit better by a bounded Warburg after discharge. One possible explanation for the difference seen in the diffusion behavior of H_xCrS_2 could be that as guest ion sites are filled during discharge the diffusion pathways become more dimensionally limited. This would explain the change to bounded Warburg behavior seen at deeper discharges. The difference in Warburg behavior in the Nyquist plots indicates a differing diffusion mechanism in the H_xCrS_2 at deeper discharge states. Impedance spectra were also collected for cycling versus Li/Li^+ and show similar behavior but with higher impedances and slower diffusion than experiments with Na counter electrodes (Figure S10, Supporting Information). This shows not only that the diffusion constants calculated for H_xCrS_2 are for mobile sodium ions, but also forewarns that the material exhibits poor cycling against lithium.

Galvanostatic intermittent titration (GITT) was employed to confirm the diffusion constants obtained from EIS using a method established by Nickol et al.[38] Diffusion constants (D) found with GITT closely matched those determined by EIS ($D \approx 4.5 \times 10^{-10}$ cm^2 s^{-1}). **Figure 3**a shows the titration curve with an inset of a single pulse which was used to calculate the diffusion constant at deep discharge. GITT also demonstrates that while the first discharge suffers from a large polarization, subsequent charge and discharge cycles see this decrease significantly.
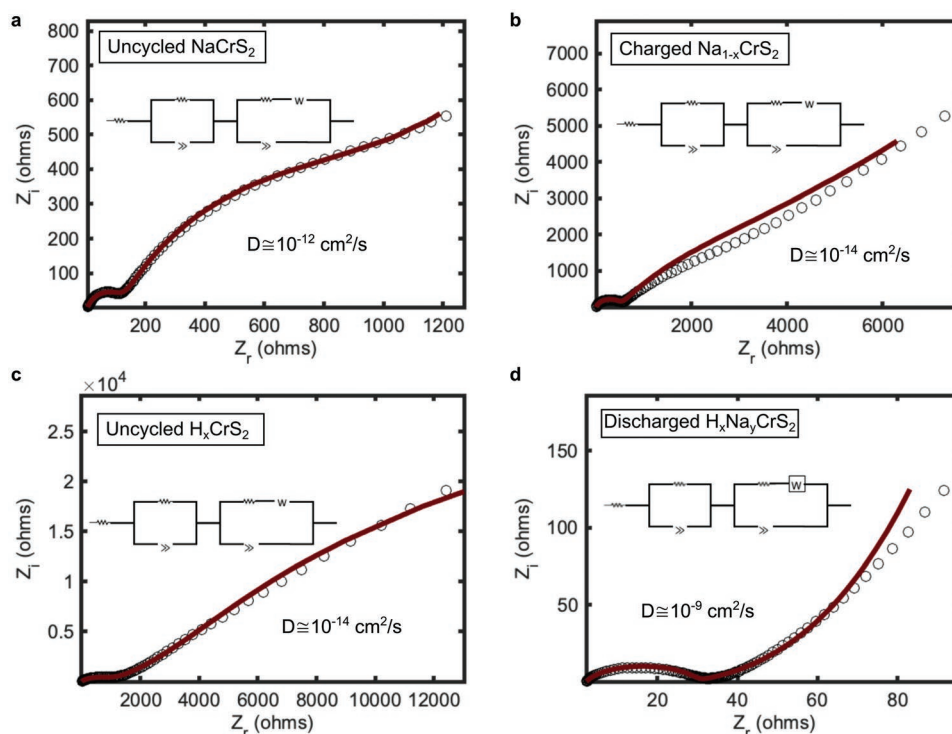
Figure 2. EIS characterization. Nyquist plots and associated fits for NaCrS$_2$ versus Na/Na$^+$ a) before and b) after the first charge and for H$_x$CrS$_2$ vs Na/Na$^+$ c) before and d) after the first discharge. These show dramatically lower impedances in the sodiated H$_x$CrS$_2$, suggesting that H$_x$CrS$_2$ exhibits fast ion diffusion. The circuits applied in the fits are shown in each panel.

Similarly, potentiostatic intermittent titration (PITT) was used to confirm fast diffusion. By fitting the current decays at each potential step, we were able to assign a diffusion constant at each potential along the curve. Diffusion constants were calculated using the simple approximation established by Vorotyntsev et al.[39] Additional details on the fitting process of GITT and PITT data is provided in the Supporting Information and Figure S7, Supporting Information. Figure 3f shows the diffusion constants determined using PITT on the first charge cycle after initial discharge. Importantly, the diffusion constant never drops below 10^{-9} cm^2 s^{-1} during the charge and in fact, reaches values near 10^{-6} cm^2 s^{-1}. This is similar to the diffusion rates achieved by composite materials such as SnS$_2$/graphene sandwiches.[31] A key difference is that here fast diffusion is seen in bare H$_x$CrS$_2$ whereas bare SnS$_2$ has a diffusion constant along the order of 10^{-15} cm^2 s^{-1}.[40] The diffusion performance of H$_x$CrS$_2$ may be even further improved by future studies compositing it with materials such as graphene. We can also see the evolution of the diffusion constant follows a trend of decreasing along plateaus in the charge curve and increasing outside of those phase change regions. This is reasonable as during plateaus significant structural rearrangement is necessary.

We performed cyclic voltammetry (CV) to determine if the redox activity changes in addition to the ion transport character. Immediately evident from the CV is that the redox behavior of H$_x$CrS$_2$ differs from that of NaCrS$_2$ when they are cycled against sodium (Figure 3b). In particular, we see a stronger and more rapid evolution of a redox peak centered at 2.7 V versus Na/Na$^+$ in the H$_x$CrS$_2$ than in NaCrS$_2$ (Figure S4, Supporting

Information). This is the first sign that the mechanism of charge storage of NaCrS$_2$ is altered in H$_x$CrS$_2$. CV also indicates an increased capacity with higher normalized current densities in H$_x$CrS$_2$ compared with NaCrS$_2$. However, there are no significant additional peaks present in H$_x$CrS$_2$ CVs as compared with experiments using NaCrS$_2$. The large low voltage peak in the initial discharge is indicative of solid electrolyte interphase formation and corresponds to the long plateau in the first constant current discharge. H$_x$CrS$_2$ also features altered behavior versus Li/Li$^+$ when compared with LiCrS$_2$ except that in the lithium system, H$_x$CrS$_2$ includes a new redox peak (Figures S8 and S9, Supporting Information).

Constant current cycling in Figure 3c shows dramatic improvements in capacity retention in H$_x$CrS$_2$ when cycled versus Na/Na$^+$ over similar testing of NaCrS$_2$ which loses 40% of its capacity over the first five cycles (Figure S3, Supporting Information). The capacity fade in H$_x$CrS$_2$ is improved with minimal losses over the first 30 cycles in the same voltage window as seen in Figure 3d. H$_x$CrS$_2$ additionally features a significant increase in reversible capacity over NaCrS$_2$, achieving 728 mAh g^{-1} compared to 350 mAh g^{-1} for NaCrS$_2$ at C/10. Due to the high measured diffusion constant of H$_x$CrS$_2$, the material was also tested at higher currents. At a rate of C/2 (343 mA g^{-1}), a capacity of 480 mAh g^{-1} is maintained over 100 cycles (Figure 3e). The two phases present in H$_x$CrS$_2$ have an average stoichiometry close to H$_x$CrS$_{2.15}$, resulting in a high theoretical capacity of 755.1 mAh g^{-1} corresponding to 3.3 Na per mol. This highlights the importance of the chemical processing and the unique structural nature of H$_x$CrS$_2$. Additionally, unlike NaCrS$_2$, H$_x$CrS$_2$ is

ADVANCED
SCIENCE NEWS

www.advancedsciencenews.com
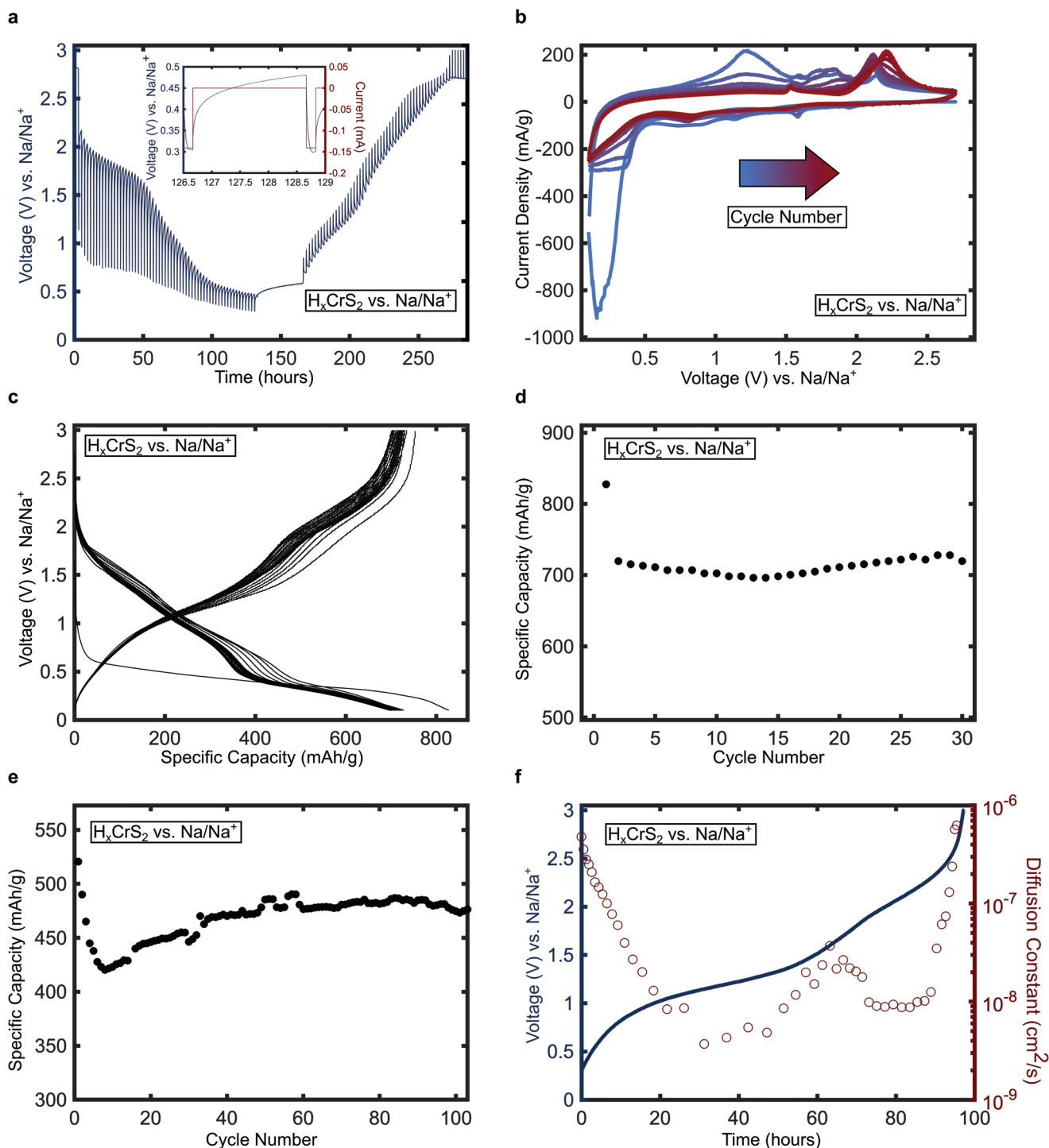
ADVANCED
MATERIALS

www.advmat.de

Figure 3. H_xCrS_2 electrochemistry. a) GITT analysis of H_xCrS_2 confirms diffusion constants from EIS. The inset shows a single constant current pulse which was used to perform diffusion calculations at a discharged state. b) Cyclic voltammetry of H_xCrS_2 shows a shift in the position of the oxidation peak following the first cycle which differs from what is seen in $NaCrS_2$. c) Galvanostatic cycling of H_xCrS_2 achieves a high capacity of 728 mAh g^{-1} at d) C/10 and e) 480 mAh g^{-1} at C/2 normalized to the mass of H_xCrS_2 which are sustained over many cycles. f) PITT analysis shows the diffusion constant evolution as a function of the first charge after initial discharge and shows that the diffusion constant remains remarkably high throughout the process.

capable of accessing nearly the entire theoretical capacity. The distinct crystalline and amorphous layers work in tandem to allow higher capacities in H_xCrS_2. To rule out contributions to the capacity from structural hydrogen in the electrode, Raman

spectra of both the uncycled and discharged material are provided in Figure S2, Supporting Information. The morphology of the material both before and after discharge was also studied using scanning electron microscopy (SEM) and is shown in
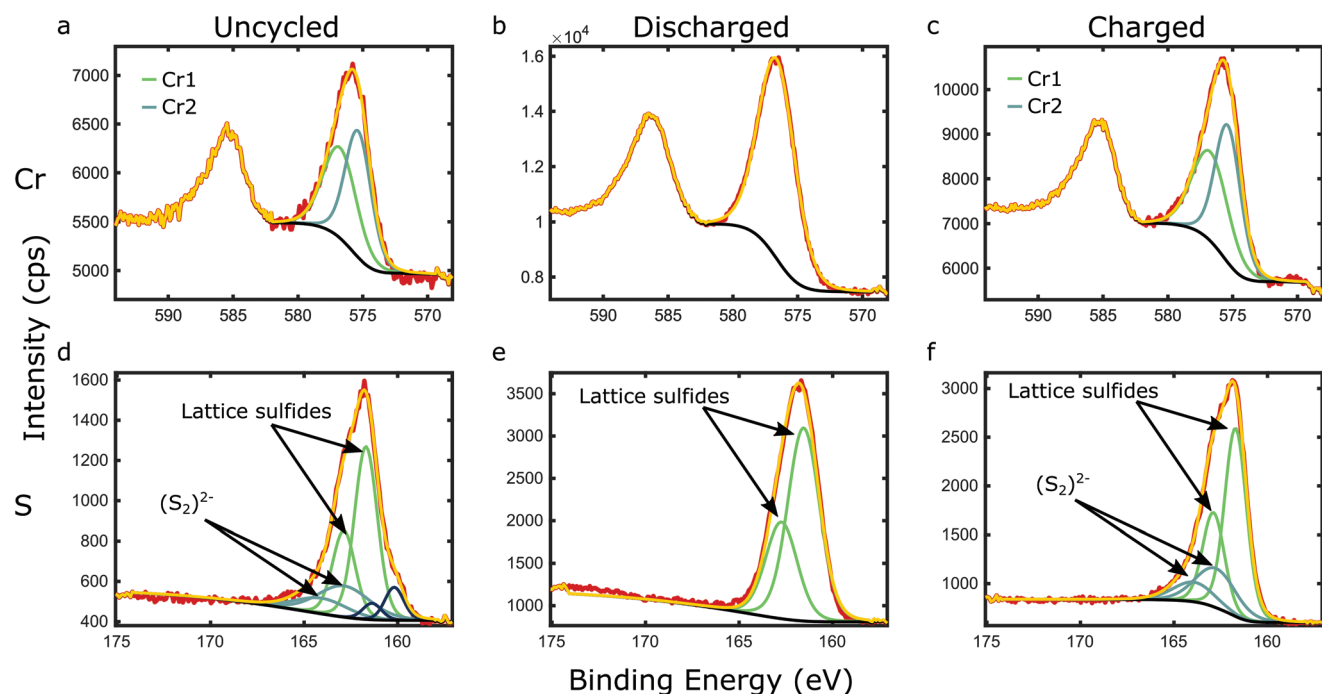
Figure 4. Ex situ X-ray photoelectron spectroscopy. a–c) 2p spectra for Cr after a) no cycling, b) first discharge, and c) subsequent charge. d–f) 2p spectra for S after d) no cycling, e) first discharge, and f) subsequent charge. These show that both Cr and S redox are accessed in H_xCrS_2.

Figure S11, Supporting Information. A full mechanistic understanding of the interplay between the two phases is beyond the scope of the current study, however, the evolution of the capacity shows some similarities to conversion electrodes. Notably, H_xCrS_2 outperforms other conversion electrodes at room temperature so the multiple phases must still elicit some improvements to the performance.

2.3. X-Ray Photoelectron Spectroscopy

We employ *ex situ* x-ray photoelectron spectroscopy (XPS) to investigate possible sources of the high measured capacity we observe in H_xCrS_2. The sample was sputtered to remove the conductive and placticizing additives that had been added to the electrode. Electrodes were studied in the uncycled state, after one discharge, and after the subsequent charge. This revealed reversible changes in both the S and Cr oxidation states, indicating that the material undergoes both cationic and anionic redox. The Cr 2p spectrum before cycling (**Figure 4**a) clearly shows two chromium states and is necessarily fit using two different curves where the $2p_{3/2}$ peaks lie at 575.48 and 576.98 eV. This is consistent with the structure of the material and corresponds to the Cr in the crystalline layer and the Cr in the amorphous layer and agrees with previous XPS data on uncycled H_xCrS_2.[24] Upon discharge in Figure 4b the spectrum is fit better by a single site and a slight increase of about 0.4 eV in the spin orbit splitting between the $2p_{3/2}$ and the $2p_{1/2}$ is observed. Changes of up to 1 eV in spin orbit splitting for Cr 2p peaks have previously been attributed to changes in chemical environment and coordination.[41–43] It additionally shows that discharge of H_xCrS_2 involves reduction of Cr. We simultaneously

observe reduction of the $(S_2)^{2-}$ dimer in Figure 4d as was seen in $NaCrS_2$ which can be seen by the lack of the single 2p pair originating from lattice sulfides. Figures 4c and 4f show the Cr and S spectra after subsequent charge and demonstrates that the changes seen on discharge are reversible, including the change in spin orbit splitting of the Cr 2p spectrum. This is evidence that our proton exchange pretreatment and the biphasic nature of H_xCrS_2 unlocks access to higher capacities through both cationic and anionic redox. Further investigation into the mechanism by which such high capacity is achieved is certainly of interest, including operando X-ray diffraction and spectroscopy experiments. Peak positions, full-width half max, and peak areas are tabulated in Table S1, Supporting Information.

3. Conclusion

We investigated the impact of proton-exchange on the electrochemical behavior of $NaCrS_2$ and found a number of significant changes. These include a change in the evolution of the oxidation process during charge, vastly improved capacity retention, and a high capacity of 728 mAh g^{-1}. It is possible that the increased capacity could be attributed to coupled cationic redox of the Cr, made accessible by chemical processing. The increased capacity and improved retention are likely due to fast diffusion of Na$^+$ through the electrode. A high diffusion constant ($D \approx 10^{-9}$ cm^{2}s^{-1}) is accompanied by a change in the mechanism by which sodium diffuses into H_xCrS_2 as supported by the change in the diffusion limitations in EIS fits.

Pretreatment of $NaCrS_2$ fully deintercalates Na from the interlayer and affects certain structural rearrangements. In particular, a migration of Cr into the Na interstitial vacancy is

observed, resulting in an amorphous layer between Cr-S crystalline slabs which is also known to impede deintercalation of Na from $NaCrS_2$.[17,24] We find that this results in a diffusion constant 4–6 orders of magnitude higher than in pristine $NaCrS_2$ when cycled against sodium. EIS fits also demonstrate that the diffusion limitations of H_xCrS_2 have different characteristics from those of $NaCrS_2$. The improvements to ion transport through H_xCrS_2 are resilient and last throughout long term cycling. The improved diffusion of H_xCrS_2 enables us to achieve the reversible (de)intercalation of three equivalents of sodium, resulting in a high, stable capacity over 700 mAh g^{-1} with a maximum of 728 mAh g^{-1}. This is the best reported performance of a sodium anode without the addition of FEC. These results show that side reactions in layered sulfide electrodes which limit capacity can be circumvented. As demonstrated by H_xCrS_2 pretreatment of layered sulfides to deintercalate the interstitial guest allows access to the full capacity of the material without hinderance by migration of the transition metal atom or irreversible formation of alkali metal sulfides.

4. Experimental Section

Synthesis and Materials Characterization: $NaCrS_2$ and H_xCrS_2 were prepared according to the methods outlined by Song et al.[24] Cr powder (Alfa Aesar, -100 mesh, 99%) was ground with a stoichiometric quantity of anhydrous Na_2S (Alfa Aesar, granular, 95%) and an excess of S powder (Alfa Aesar, -100 mesh, 99.5%) in an argon glovebox before transferring to a fused silica tube which was flushed with argon and sealed under vacuum. The tube was then placed in a furnace and heated to 700 °C at a rate of 2 °C min^{-1} and held at that temperature for 48 h before shutoff of the furnace. The resultant $NaCrS_2$ powder was washed with ethanol and water.

To produce the proton-exchanged H_xCrS_2, the $NaCrS_2$ precursor was first synthesized and then subjected to shaking in a solution of 1 M HCl in 25% H_2O in ethanol for 4 days, filtering and changing out the solution each day. After the 4 days, the powder was filtered again, washed with ethanol and annealed at 150 °C for 72 h. Early experiments demonstrated that this annealing step is essential to the electrochemistry. The purity of both $NaCrS_2$ and H_xCrS_2 was confirmed using X-ray diffraction (XRD) on an in house STOE STADI P diffractometer.

Electrode Preparation: After successful synthesis and confirmation of phase purity, the materials were cast as slurry electrodes. Active material was mixed with carboxymethylcellulose (CMC) (Sigma-Aldrich, Mw 250 000) as a binder and C-Nergy Super 65 Carbon (surface area = 62 m^2 g^{-1}) as a conductive additive in a mass ratio of 80:10:10 before mixing with water to produce a slurry. The slurry was cast on a copper current collector with a thickness of 30 μm, and area of 0.97 cm^2, and a typical mass on the order of 2.5 mg. After drying, the electrode slurries were punched out and put into 304SS CR2032 coin cells for testing. These coin cells used Celgard 2320 separators and sodium metal combined counter-reference electrodes. The electrolyte was 1 M $NaPF_6$ (Alfa Aesar, 98%) in bis(2-methoxyethyl) ether (diglyme) (Alfa Aesar, 99%).

Electrochemical and Ex Situ Characterization: A number of electrochemical tests were performed to assess the performance of the electrodes including electrochemical impedance spectroscopy (EIS), galvanostatic intermittent titration technique (GITT), potentiostatic intermittent titration technique (PITT), cyclic voltammetry (CV), and galvanostatic cycling with potential limitation (GCPL). EIS measurements were performed at the terminus of a charge or discharge over a frequency range of 0.01 Hz to 1 MHz using a 10 mV voltage perturbation. CVs were performed with a scan rate of 0.1 mV s^{-1}. In the GCPL experiments, an assumption of (de)intercalation of three guest ions was made to determine theoretical capacity and a current of C/15, corresponding to about 76 mA g^{-1} or 0.21 mA cm^{-2} was used based on those calculations. Cycling experiments operated versus a sodium reference were done in a 0.1–3.0 V versus Na/Na$^+$ potential range. Between each charge and discharge of the GCPL an EIS measurement was taken. GITT measurements were taken using a current rate of C/10 with 10 min pulses and a relaxation period of up to 2 h. PITT measurements used 5 mV potential steps with an acceleration current of C/100 and fits of the diffusion constant were made for the first charge after initial discharge.

Electrochemical experiments were performed on a slate of instruments. Long constant-current cycling experiments were done using a 16 channel Arbin MSTAT. EIS experiments, including cycling with EIS, were performed on a Gamry Interface 1000E and analysis was performed using the Gamry software Echem Analysis. Fits of Nyquist plots were also performed in the Gamry software. This yielded a diffusion coefficient which was used to calculate diffusion constants as described in Supporting Information. Electrochemical titration experiments and CVs were performed using a Biologic SP-150 and analysis was performed using EC-Lab.

Ex-situ XPS measurements were conducted after discharge and charge using a Thermo Scientific K-Alpha XPS system. For these experiments, a rate of C/10 was used and the electrodes were harvested then washed with diglyme and hexane before being introduced to the XPS. Sample preparation was done in an argon glove box and the samples were transferred to the XPS using a vacuum transfer module to prevent contamination from the air. Collected spectra were fit using CasaXPS.

Supporting Information

Supporting Information is available from the Wiley Online Library or from the author.

Conflict of Interest

The authors declare no conflict of interest.

Data Availability Statement

The data that support the findings of this study are available from the corresponding author upon reasonable request.

**ADVANCED
SCIENCE NEWS**

www.advancedsciencenews.com

**ADVANCED
MATERIALS**

www.advmat.de

[1] J.-M. Tarascon, *Nat. Chem.* **2010**, *2*, 510.

[2] J.-Y. Hwang, S.-T. Myung, Y.-K. Sun, *Chem. Soc. Rev.* **2017**, *46*, 3529.

[3] B. W. Jaskula, US Geological Survey Mineral Commodity Summaries (Reston, VA: US Department of the Interior and US Geological Survey, 2011), https://d9-wret.s3.us-west-2.amazonaws.com/assets/palladium/production/mineral-pubs/lithium/mcs-2011-lithi.pdf (accessed: April 2021).

[4] D. B. Agusdinata, W. Liu, H. Eakin, H. Romero, *Environ. Res. Lett.* **2018**, *13*, 123001.

[5] N. Tapia-Ruiz, A. R. Armstrong, H. Alptekin, M. A. Amores, H. Au, J. Barker, R. Boston, W. R. Brant, J. M. Brittain, Y. Chen, M. Chhowalla, Y.-S. Choi, S. I. R. Costa, M. C. Ribadeneyra, S. A. Cussen, E. J. Cussen, W. I. F. David, A. V. Desai, S. A. M. Dickson, E. I. Eweka, J. D. Forero-Saboya, C. P. Grey, J. M. Griffin, P. Gross, X. Hua, J. T. S. Irvine, P. Johansson, M. O. Jones, M. Karlsmo, E. Kendrick, et al., *J. Phys.: Energy* **2021**, *3*, 031503.

[6] Y. Kim, Y. Kim, A. Choi, S. Woo, D. Mok, N.-S. Choi, Y. S. Jung, J. H. Ryu, S. M. Oh, K. T. Lee, *Adv. Mater.* **2014**, *26*, 4139.

[7] D. C. Hannah, G. Sai Gautam, P. Canepa, G. Ceder, *Adv. Energy Mater.* **2018**, *8*, 1800379.

[8] M. Liu, A. Jain, Z. Rong, X. Qu, P. Canepa, R. Malik, G. Ceder, K. A. Persson, *Energy Environ. Sci.* **2016**, *9*, 3201.

[9] C. J. Hansen, J. J. Zak, A. J. Martinolich, J. S. Ko, N. H. Bashian, F. Kaboudvand, A. Van der Ven, B. C. Melot, J. Nelson Weker, K. A. See, *J. Am. Chem. Soc.* **2020**, *142*, 6737.

[10] M. S. Whittingham, *Science* **1976**, *192*, 1126.

[11] Y. Kim, K.-s. Park, S.-h. Song, J. Han, J. B. Goodenough, *J. Electrochem. Soc.* **2009**, *156*, A703.

[12] Y. Kim, K.-H. Ha, S. M. Oh, K. T. Lee, *Chem. - Eur. J.* **2014**, *20*, 11980.

[13] F. Klein, B. Jache, A. Bhide, P. Adelhelm, *Phys. Chem. Chem. Phys.* **2013**, *15*, 15876.

[14] L. Chen, M. Fiore, J. E. Wang, R. Ruffo, D.-K. Kim, G. Longoni, *Adv. Sustainable Syst.* **2018**, *2*, 1700153.

[15] P. Canepa, G. Sai Gautam, D. C. Hannah, R. Malik, M. Liu, K. G. Gallagher, K. A. Persson, G. Ceder, *Chem. Rev.* **2017**, *117*, 4287.

[16] M. R. Habib, S. Wang, W. Wang, H. Xiao, S. M. Obaidulla, A. Gayen, Y. Khan, H. Chen, M. Xu, *Nanoscale* **2019**, *11*, 20123.

[17] Z. Shadike, Y.-N. Zhou, L.-L. Chen, Q. Wu, J.-L. Yue, N. Zhang, X.-Q. Yang, L. Gu, X.-S. Liu, S.-Q. Shi, Z.-W. Fu, *Nat. Commun.* **2017**, *8*, 566.

[18] K. Luo, M. R. Roberts, R. Hao, N. Guerrini, D. M. Pickup, Y.-S. Liu, K. Edström, J. Guo, A. V. Chadwick, L. C. Duda, P. G. Bruce, *Nat. Chem.* **2016**, *8*, 684.

[19] M. Sathiya, G. Rousse, K. Ramesha, C. Laisa, H. Vezin, M. T. Sougrati, M.-L. Doublet, D. Foix, D. Gonbeau, W. Walker, A. S. Prakash, M. Ben Hassine, L. Dupont, J.-M. Tarascon, *Nat. Mater.* **2013**, *12*, 827.

[20] M. Sathiya, A. M. Abakumov, D. Foix, G. Rousse, K. Ramesha, M. Saubanère, M. Doublet, H. Vezin, C. Laisa, A. Prakash, D. Gonbeau, G. VanTendeloo, J.-M. Tarascon, *Nat. Mater.* **2015**, *14*, 230.

[21] E. McCalla, M. T. Sougrati, G. Rousse, E. J. Berg, A. Abakumov, N. Recham, K. Ramesha, M. Sathiya, R. Dominko, G. Van Tendeloo, P. Novák, J.-M. Tarascon, *J. Am. Chem. Soc.* **2015**, *137*, 4804.

[22] E. McCalla, A. M. Abakumov, M. Saubanère, D. Foix, E. J. Berg, G. Rousse, M.-L. Doublet, D. Gonbeau, P. Novák, G. Van Tendeloo, R. Dominko, J.-M. Tarascon, *Science* **2015**, *350*, 1516.

[23] G. Assat, J.-M. Tarascon, *Nat. Energy* **2018**, *3*, 373.

[24] X. Song, G. Cheng, D. Weber, F. Pielnhofer, S. Lei, S. Klemenz, Y.-W. Yeh, K. A. Filsinger, C. B. Arnold, N. Yao, L. M. Schoop, *J. Am. Chem. Soc.* **2019**, *141*, 15634.

[25] M. Indrikova, S. Grunwald, F. Golks, A. Netz, B. Westphal, A. Kwade, *J. Electrochem. Soc.* **2015**, *162*, A2021.

[26] Q. Cheng, T. Yang, Y. Li, M. Li, C. K. Chan, *J. Mater. Chem. A* **2016**, *4*, 6902.

[27] Q. Cheng, T. Yang, M. Li, C. K. Chan, *Langmuir* **2017**, *33*, 9271.

[28] Y. Liang, H. D. Yoo, Y. Li, J. Shuai, H. A. Calderon, F. C. Robles Hernandez, L. C. Grabow, Y. Yao, *Nano Lett.* **2015**, *15*, 2194.

[29] C. Yang, X. Ou, X. Xiong, F. Zheng, R. Hu, Y. Chen, M. Liu, K. Huang, *Energy Environ. Sci.* **2017**, *10*, 107.

[30] X. Xiong, C. Yang, G. Wang, Y. Lin, X. Ou, J.-H. Wang, B. Zhao, M. Liu, Z. Lin, K. Huang, *Energy Environ. Sci.* **2017**, *10*, 1757.

[31] Y. Jiang, D. Song, J. Wu, Z. Wang, S. Huang, Y. Xu, Z. Chen, B. Zhao, J. Zhang, *ACS Nano* **2019**, *13*, 9100.

[32] L. Cao, X. Liang, X. Ou, X. Yang, Y. Li, C. Yang, Z. Lin, M. Liu, *Adv. Funct. Mater.* **2020**, *30*, 1910732.

[33] Y. Chen, H. Liu, X. Guo, S. Zhu, Y. Zhao, S. Iikubo, T. Ma, *ACS Appl. Mater. Interfaces* **2021**, *13*, 39248.

[34] M. M. Butala, M. Mayo, V. V. Doan-Nguyen, M. A. Lumley, C. Göbel, K. M. Wiaderek, O. J. Borkiewicz, K. W. Chapman, P. J. Chupas, M. Balasubramanian, G. Laurita, S. Britto, A. J. Morris, C. P. Grey, R. Seshadri, *Chem. Mater.* **2017**, *29*, 3070.

[35] S. J. Hibble, R. I. Walton, D. M. Pickup, *J. Chem. Soc., Dalton Trans.* **1996**, *11*, 2245.

[36] W. Wang, S. Wang, H. Jiao, P. Zhan, S. Jiao, *Phys. Chem. Chem. Phys.* **2015**, *17*, 4551.

[37] U. Westerhoff, K. Kurbach, F. Lienesch, M. Kurrat, *Energy Technol.* **2016**, *4*, 1620.

[38] A. Nickol, T. Schied, C. Heubner, M. Schneider, A. Michaelis, M. Bobeth, G. Cuniberti, *J. Electrochem. Soc.* **2020**, *167*, 090546.

[39] M. A. Vorotyntsev, M. D. Levi, D. Aurbach, *J. Electroanal. Chem.* **2004**, *572*, 299.

[40] P. Zhou, X. Wang, W. Guan, D. Zhang, L. Fang, Y. Jiang, *ACS Appl. Mater. Interfaces* **2017**, *9*, 6979.

[41] C. Fisk, C. Valdemoro, S. Fraga, *J. Chem. Phys.* **1968**, *48*, 2923.

[42] G. Allen, P. Tucker, *Inorg. Chim. Acta* **1976**, *16*, 41.

[43] D. Briggs, *Practical Surface Analysis, Auger and X-Ray Photoelecton Spectroscopy* **1990**, *1*, 151.